



Mid-infrared laser absorption tomography for quantitative 2D thermochemistry measurements in premixed jet flames

Chuyu Wei¹ · Daniel I. Pineda¹ · Laurel Paxton² · Fokion N. Egolfopoulos² · R. Mitchell Spearrin¹

Received: 1 February 2018 / Accepted: 18 May 2018 / Published online: 30 May 2018
© Springer-Verlag GmbH Germany, part of Springer Nature 2018

Abstract

A tomographic laser absorption spectroscopy technique, utilizing mid-infrared light sources, is presented as a quantitative method to spatially resolve species and temperature profiles in small-diameter reacting flows relevant to combustion systems. Here, tunable quantum and interband cascade lasers are used to spectrally resolve select rovibrational transitions near 4.98 and 4.19 μm to measure CO and CO₂, respectively, as well as their vibrational temperatures, in piloted premixed jet flames. Signal processing methods are detailed for the reconstruction of axial and radial profiles of thermochemical structure in a canonical ethylene–air jet flame. The method is further demonstrated to quantitatively distinguish between different turbulent flow conditions.

1 Introduction

Most practical combustion devices involve turbulent reacting flows. Understanding interactions between chemistry and fluid dynamics in turbulent flames is of prime interest to the combustion community, both for the development of more efficient engineering devices and the development and refinement of numerical models [1]. As computational power increases and higher fidelity simulations of turbulent flames with more detailed chemistry become possible, it is necessary to provide measurements to inform and anchor these models [2]. Specifically, quantitative measurements of the thermochemical structure (i.e., spatially resolved species and temperature) are needed to elucidate the coupled mechanisms.

Traditional intrusive measurement techniques such as thermocouples and gas chromatography (using sampling

probes) disturb the local flow field, often precluding definitive interpretation. As such, several non-intrusive spectroscopic measurement techniques have been utilized to study turbulent flames by exploiting emission, absorption, and scattering interactions. For turbulent jet flames, which are the focus of this work, Rayleigh scattering has been a common approach for thermometry [3–5], and can be quantitative with an estimation of gas composition [6–8]. Raman scattering methods have also been used for time-resolved point measurements of species in such flames [9–11]; however, this approach does not readily lend towards characterizing the structure of a flame unless many point measurements are made [12, 13], which can be difficult to perform if the burner is immobile and the lasers are large and cumbersome, which is often the case with high-powered light sources required in scattering spectroscopies. Laser-induced fluorescence (LIF) [10, 14–16] and chemiluminescence [15, 17, 18] have also been used extensively for temperature and species-specific imaging. However, these methods do not easily yield quantitative species measurements, even with calibrations [19].

Although typically weak in spatial resolution capability (due to line-of-sight integration), laser absorption spectroscopy (LAS) provides a highly quantitative, calibration-free method of measuring major combustion species and temperature in harsh environments using compact low-power semiconductor lasers [20]. Room-temperature interband cascade lasers (ICLs) and quantum cascade lasers (QCLs) enable convenient access to the strong mid-infrared (mid-IR)

This article is part of the topical collection “Mid-infrared and THz Laser Sources and Applications” guest edited by Wei Ren, Paolo De Natale and Gerard Wysocki.

✉ Chuyu Wei
weicy@ucla.edu

¹ Department of Mechanical and Aerospace Engineering, University of California, Los Angeles, Los Angeles, CA 90095, USA

² Department of Aerospace and Mechanical Engineering, University of Southern California, Los Angeles, CA 90089, USA

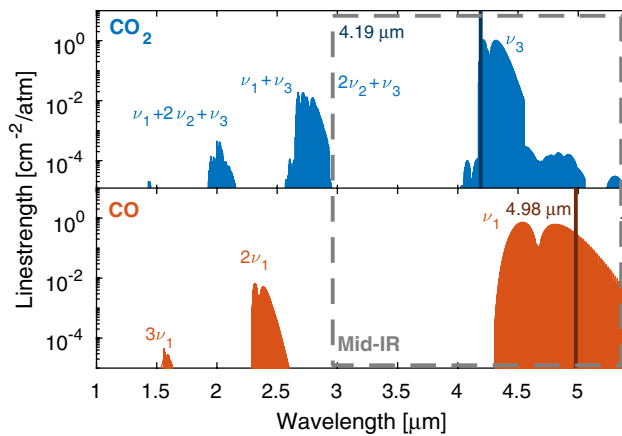


Fig. 1 Absorption line strengths for CO₂ (top) and CO (bottom) from 1 to 5 μm computed from the HITRAN database [21]; $T = 1500$ K. Fundamental vibrational bands ν_i as well as combinations of these bands are labeled for each species. Accessible regions in mid-infrared wavelengths due to the recent availability of mid-infrared ICLs and QCLs are marked with a gray dashed box. Wavelengths specifically used in this study are marked with darker lines

absorption bands of CO and CO₂ centered near 4.7 and 4.3 μm, respectively, as shown in Fig. 1. The fundamental vibrational bands at these mid-IR wavelengths are orders of magnitude stronger than those in the near-IR, and provide much greater species sensitivity at short optical path lengths, making them suitable for analyzing small-diameter flows in practical combustion applications. By carefully selecting the wavelength, it is possible to measure multiple absorption transitions of a single molecule with one laser, enabling simultaneous calibration-free thermometry and species concentration measurements [22].

The compactness and mobility of modern ICLs and QCLs readily enable spatially resolved measurements in flames, which can be combined with tomographic reconstruction techniques [23, 24] to characterize non-uniform flows [25–31]. In this paper, we present a stage-mounted multi-laser absorption system for quantitative measurement of species concentrations and temperature distributions in turbulent premixed jet flames.

1.1 Theory of laser absorption spectroscopy

Laser absorption spectroscopy (LAS) exploits resonance with discrete energy modes of gas molecules to ascertain thermochemical properties of flow fields from light absorption [19]. We briefly review the fundamentals of LAS here in the context of the experiment to provide reader assistance with the measurements that follow.

The Beer–Lambert law in Eq. 1 gives the spectral absorbance α_ν in a gas medium axially symmetric about radius r

[cm] for a specific frequency ν [cm⁻¹] as a function the ratio of incident light, I_0 , and the transmitted light, I_t [19]:

$$\alpha_\nu = -\ln\left(\frac{I_t}{I_0}\right)_\nu = \int_0^{L(r)} PS_j(T(r))X_{\text{abs}}(r)\varphi_\nu dl. \quad (1)$$

α_ν thus depends on total pressure P [atm], line strength S_j [cm⁻²/atm] for rovibrational transition j , mole fraction of absorbing species X_{abs} , line shape function φ_ν [cm], and aggregate path length $L(r)$ [cm]. For an integrated line-of-sight (LOS) absorption measurement through a non-uniform medium (such as a flame) that is axially symmetric in r , the projected integrated absorbance area $A_{j,\text{proj}}(r)$ [cm⁻¹] is expressed in the following equation:

$$\begin{aligned} A_{j,\text{proj}}(r) &= \int_{-\infty}^{\infty} \alpha_\nu d\nu = \int_0^{L(r)} K_j(r) dl \\ &= P \int_0^{L(r)} S_j(T(r))X_{\text{abs}}(r) dl, \end{aligned} \quad (2)$$

where P is assumed constant throughout the medium. In this work, we attained $A_{j,\text{proj}}(r)$ by fitting a Voigt function to the measured α_ν for each line j , effectively negating the measurement dependence on line shape φ_ν [19]. To determine a radial profile of the integrated spectral absorption coefficient, $K_j(r)$ [cm⁻²], from radially resolved projected area measurements $A_{j,\text{proj}}(r)$, we use tomographic reconstruction methods discussed in greater detail in Sect. 3.3. For multiple transitions j scanned, multiple $K_j(r)$ can be determined, and the ratio of two absorption coefficients reduces to a ratio of $S_j(r)$, which is a function of $T(r)$ only, as shown in the following equation:

$$R(r) = \frac{K_A(r)}{K_B(r)} = \frac{S_A(T(r))}{S_B(T(r))} = f(T(r)). \quad (3)$$

Since $S_j(T(r))$ is a line-specific spectroscopic property, it is possible to infer the gas temperature $T(r)$ with the simultaneous measure of two lines at any location r [22]. After temperature has been determined, $S_j(T(r))$ can be evaluated, and the mole fraction of the absorbing species $X_{\text{abs}}(r)$ can be obtained using Eq. 4 when the total pressure P is known. More detail on these calculations as well as their uncertainties can be found in the Appendix.

$$K_j(r) = PS_j(T(r))X_{\text{abs}}(r). \quad (4)$$

2 Method

We employ a scanned-wavelength direct-absorption technique with a tunable quantum cascade laser and an inter-band cascade laser to spectrally resolve transitions near the

Table 1 Spectroscopic parameters for targeted CO₂ transitions

| Line (ν'' , J'') | Wavelength (nm) | Freq. (cm ⁻¹) | E'' (cm ⁻¹) | S (296 K) (cm ⁻² /atm) |
|--------------------------|-----------------|---------------------------|---------------------------|-------------------------------------|
| $R(0,58)$ | 4194.30 | 2384.189 | 1333 | 7.78×10^{-1} |
| $R(1,105)$ | 4194.06 | 2384.327 | 4998 | 2.51×10^{-8} |
| $R(1,106)$ | 4194.05 | 2384.331 | 5087 | 1.65×10^{-8} |

Table 2 Spectroscopic parameters for targeted CO transitions

| Line (ν'' , J'') | Wavelength (nm) | Freq. (cm ⁻¹) | E'' (cm ⁻¹) | S (296 K) (cm ⁻² /atm) |
|--------------------------|-----------------|---------------------------|---------------------------|-------------------------------------|
| $P(1,26)$ | 4983 | 2006.78 | 3,478 | 5.20×10^{-6} |
| $P(0,31)$ | 4979 | 2008.53 | 1,901 | 6.62×10^{-3} |

fundamental bands of CO and CO₂ near 4.9 and 4.2 μm , respectively. Using mechanical translation stages and tomographic reconstruction techniques, we provide radial profiles of CO and CO₂ mole fraction as well as gas temperature for two different turbulent flow conditions in a piloted premixed jet flame burner.

2.1 Wavelength selection

For this and other combustion studies, specific wavelengths within each vibrational band of both CO₂ and CO were selected based on the isolation, strength, and temperature sensitivity of the rovibrational lines, in addition to laser availability. We probe the $P(0,31)$ and $P(1,26)$ lines of the fundamental band of CO, around 2008.53 and 2006.78 cm⁻¹, respectively, to infer CO vibrational temperature and CO mole fraction. For CO₂, we probe the $R(0,58)$ line at 2384.189 cm⁻¹, as well as the doublet line pair $R(1,105)$ and $R(1,106)$ at 2384.327 and 2384.331 cm⁻¹, respectively, to measure CO₂ mole fraction and vibrational temperature. Relevant spectroscopic parameters of the selected lines are shown in Tables 1 and 2, where line strength and lower state energy values for CO and CO₂ are taken from the HITEMP 2010 database [21]. Further details on line selection within these domains are described in previous studies [22, 32].

2.2 Laser absorption tomography system

As noted, the medium in which we attain the measurements is non-uniform, though it is assumed to be axially symmetric over a short time interval [17]. In this section, we describe the system used to mechanically obtain spatial resolution for the LAS measurements. Figure 2 shows the optical configuration around the piloted premixed jet flame burner at the University of Southern California, as well as the directions of radial and vertical translation.

A stage-mounted two-laser system was developed to measure species profiles of CO and CO₂, respectively, as well as temperature in the radial and vertical directions to characterize the time-averaged thermochemical structure of

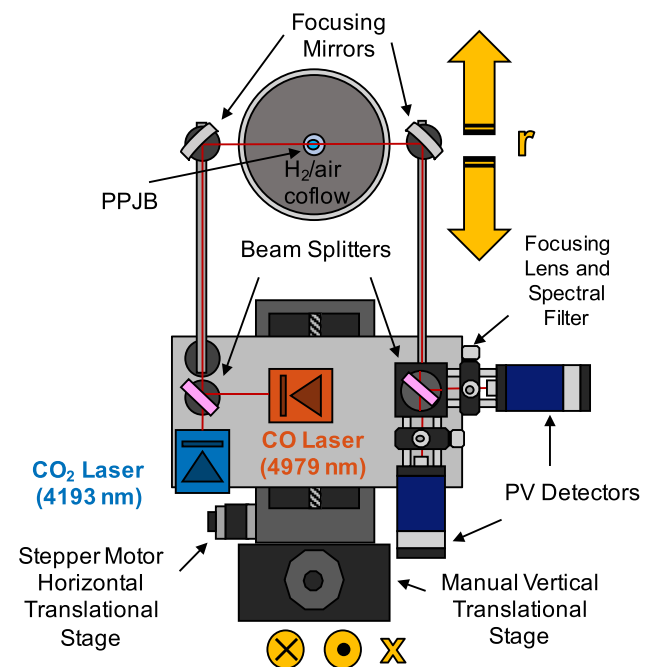


Fig. 2 Top-down schematic of the PPIB with optomechanical translation stage system. The central jet is surrounded by a co-flow H₂/air flame. The lasers, optics, and detectors are mounted to the same translational stages and move together while the burner remains stationary

the flame. A distributed-feedback (DFB) quantum cascade laser (QCL) with ≈ 50 mW output power was utilized as the single-mode light source to resolve the selected CO lines and infer thermochemical properties of CO. An interband cascade laser (ICL) with ≈ 5 mW output power is similarly used for probing the CO₂ lines. The laser beams were aligned concentrically using flat mirrors and beam splitters as shown in Fig. 2. Focusing mirrors ($f = 200$ mm) 400 mm apart were deployed on optical rails attached to the stage to focus the concentric beams to approximately 0.5 mm in diameter across the central jet. After reflection back towards the detectors, we used another beam splitter in conjunction with bandpass spectral filters (4210 nm for CO₂, 5000 nm for CO)

and focusing lenses to separate the different wavelengths onto independent detectors. The lasers, mirrors, lenses, and detectors were all mounted on a $\sim 16 \text{ cm} \times 16 \text{ cm}$ optical breadboard on an automatic radial (horizontal) translation stage, which itself was mounted on a manual vertical translation stage. The horizontal translation stage was controlled by a stepper motor with a controllable linear translation resolution of $1.6 \mu\text{m}$ per motor step in the r direction, as indicated in Fig. 2. The hand-cranked vertical translation stage had a linear translation resolution of 1.27 mm in the x -direction per lead screw revolution. Signals from the stepper motor encoder were recorded alongside the signals from the photovoltaic detectors. Additionally, the stepper motor was operated with a stepping frequency that was a sub-multiple (500 Hz) of the laser scan rate so that the r location of the laser beams could be easily tracked.

2.3 Piloted premixed jet flame burner

A discussion of the operating characteristics of the University of Southern California burner is presented here for ease of reader understanding in the sections that follow. The current work utilized a modified Piloted Premixed Jet flame Burner (PPJB) design [4] as described in greater detail in previous studies [17, 18]. The burner consists of a central jet tube of inner diameter $D = 5.84 \text{ mm}$ surrounded by a pilot and outer co-flow ($D_{\text{co-flow}} = 400 \text{ mm}$) to stabilize the high-velocity central jet. A schematic of the configuration with the laser absorption system is shown in Fig. 2. The pilot flame anchors the central jet to the burner exit to prevent blowoff from the high shear present. The pilot flame is a premixed $\text{C}_2\text{H}_4/\text{air}$ flame stabilized beneath the jet flame with an equivalence ratio of $\phi = 0.8$ and an unburnt exit velocity of 0.75 m/s .

The co-flow surrounds the pilot and jet flow, using hot products to thermally insulate the jet. A pure H_2/air flame at $\phi = 0.51$ was used to provide a surrounding temperature of $T_{\text{co-flow}} = 1500 \text{ K}$. This co-flow flame composition was chosen to provide hot products without carbon atoms present so as to provide zero concentration boundary conditions for the CO and CO_2 mole fraction reconstruction efforts. Experiments were performed at two jet Reynolds numbers, $Re_{\text{jet}} \equiv U_{\text{jet}}D/v_{\text{visc}} = 25,000$ and $50,000$, where U_{jet} is the bulk flow velocity and v_{visc} is the kinematic viscosity at the burner exit. The co-flow velocity does not change across the Reynolds number conditions. The mixture composition of the central jet is $\text{C}_2\text{H}_4/\text{air}$ at $\phi = 0.55$ and an unburned mixture temperature of 298 K . As mentioned, over a modest time interval ($\sim 10^2 \text{ ms}$), the turbulent jet can generally be approximated as axially symmetric and steady [17].

2.4 Experimental procedure

To determine the center of the jet ($r = 0$) for initial alignment, the laser beams were adjusted in the r direction across the central jet tube using the automatic horizontal stage. Locations where the detected light intensity decreased to $\sim 20\%$ of the unblocked intensity due to the obstruction of the jet tube were noted, and the location of the jet center was then determined by radial symmetry. Both the CO and CO_2 lasers were scanned at a frequency of 1 kHz , and were recorded at a sample rate of 2 MHz , as shown in Fig. 3. For the QCL, the targeted CO transitions could not be accessed with a single laser sweep at a given laser operating temperature; therefore, the CO lines were measured by sequential horizontal scans at different laser operating temperatures, at each height x above the jet exit. The CO laser operating conditions were changed and stabilized in $\sim 30\text{-s}$ intervals between the two horizontal scans. Since the experiment under investigation is quasi-steady [17], this was considered an acceptable method to capture both CO transitions. The stepper motor encoder signals from the automatic horizontal translation stage were also recorded at the same frequency. The horizontal translation speed was 0.8 mm/s , resulting in two laser scans per $1.6 \mu\text{m}$ step. To measure the baseline signal I_0 , background measurements were taken with the lasers during an automatic horizontal translation while the H_2/air co-flow of the burner was on, but without any hydrocarbon fuels flowing, for every r position at the minimum and maximum x locations for the flame. These background measurements with the hot co-flow gases account for incident effects from environmental thermal emission and water

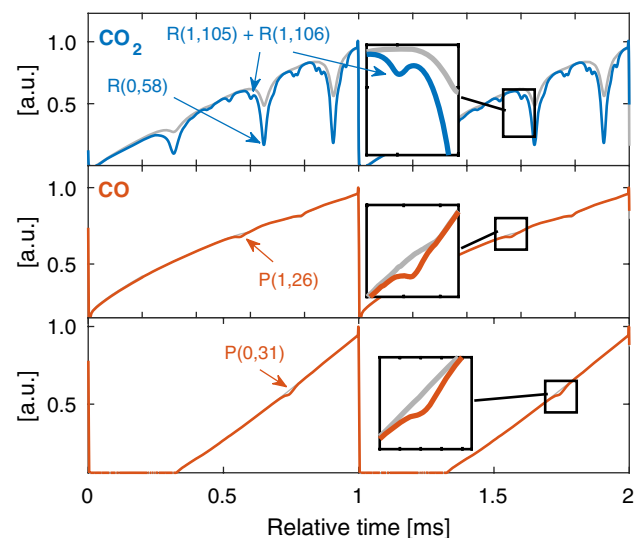


Fig. 3 Example of direct-absorption scans for selected CO_2 and CO lines (I_t) with specific transitions labeled. Gray lines indicate background signals (I_0) with the $\text{C}_2\text{H}_4/\text{air}$ jet flame and pilot turned off but with the hot co-flow H_2/air on

absorption, as well as CO_2 in the ambient air. No significant differences in absorption were observed using either x location background measurement. As the burner was operating, finely resolved horizontal scans in the r -direction were made every 20 mm in height above the burner exit. The system was translated as far as $r = 32$ mm to ensure zero concentration boundary conditions for later reconstruction efforts, as detailed in Sect. 3.3. Once a translation was completed for a given r - x combination, the horizontal stage was returned to the $r = 0$ location and the vertical translation stage was adjusted in the x -direction to a new height above the jet exit. This process was repeated for several axial locations x along the flame. For the case in which $Re = 25,000$, fewer x locations were scanned since the flame was shorter. This simultaneous translation and data acquisition method was chosen to maximize spatial data collection of the mean flow properties during the available test time.

3 Data analysis

This section presents the methods we employed to interpret the measurements obtained in the experiment into axial and radial profiles of temperature and species measurements. For the results shown here, 105 direct-absorption scans (Fig. 3) associated with a horizontal translation interval were averaged prior to the calculation of projected absorbance area $A_{j,\text{proj}}(r)$ via Eqs. 1 and 2. This procedure is done for each spatial interval throughout the horizontal scan and allows for statistical analysis of the signals in the interval. We determine the 95% confidence interval of all of these signals, and use this information to process the uncertainty in the rest of our results. The uncertainty analysis is presented in greater detail in the Appendix.

3.1 Spectral line fitting

The measured absorbance spectra α_ν are least-squares fit for the target spectral lines in Tables 1 and 2 using the Voigt line shape function [19] to obtain projected absorbance areas $A_{j,\text{proj}}(r)$, as shown in Figs. 4 and 5 for CO_2 and CO , respectively. $A_{j,\text{proj}}(r)$ and collisional width ν_c were free parameters for the fitting process, and Doppler width ν_D was assumed corresponding to the co-flow temperature of 1500 K. It was noted that when arbitrarily assuming the temperature (from 500 to 1500 K) for the Doppler width, there was no discernible difference for the integrated area results, which are used for tomographic reconstruction.

Due to the large difference in line strength between the targeted CO_2 spectral lines, the regular two-line fitting procedure is not robust enough for reliably simultaneously fitting the $R(0,58)$ line and the $R(1,105) + R(1,106)$ doublet line without significantly biasing the fitting of the $R(1,105) +$

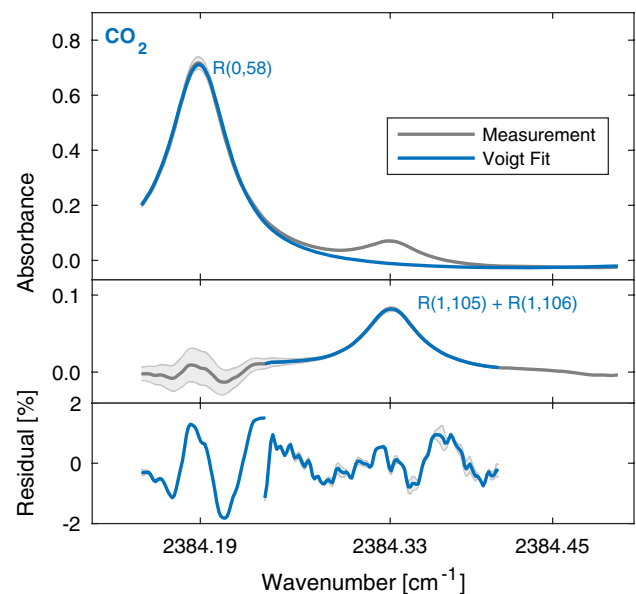


Fig. 4 Measured carbon dioxide absorption averaged from 105 laser scans (1 kHz) shown as absorbance versus wave number for the $R(0,58)$ line and the $R(1,105) + R(1,106)$ doublet line. 95% confidence interval of measured absorbance shown in gray. Top: Voigt fit of solely the $R(0,58)$ line. Middle: Voigt fit of the $R(1,105) + R(1,106)$ doublet calculated from the difference between the measured data and the $R(0,58)$ fit. Bottom: residuals from each of the above Voigt fits. Variation in residuals from fitting within the bound of experimental uncertainty are shown in gray

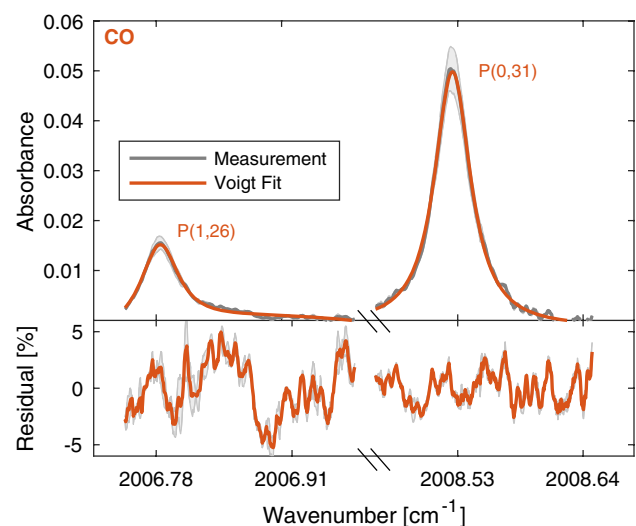


Fig. 5 Top: measured carbon monoxide absorption averaged from 105 laser scans (1 kHz) shown as absorbance versus wave number for the $P(1,26)$ and the $P(0,31)$ lines. 95% confidence interval of measured absorbance shown in gray. Bottom: residuals from Voigt fit. Variation in residuals from fitting within the bound of experimental uncertainty are shown in gray

$R(1,106)$ doublet line. For this reason, we adopted a sequential fitting routine in which the $R(0,58)$ line was fit first for a specified data range (top of Fig. 4) after confirming that this range did not bias the $A_{j,proj}(r)$ results compared to successful simultaneous fits with the $R(1,105) + R(1,106)$ doublet line. This Voigt fit for the $R(0,58)$ line was then subtracted from the original measured spectral absorbance α_v to generate a residual measurement of only the $R(1,105) + R(1,106)$ doublet line (middle of Fig. 4). This residual spectral absorbance was then fit to extract $A_{j,proj}(r)$ from the $R(1,105) + R(1,106)$ doublet line. The final fractional residual (residual / maximum absorbance) resulting from the Voigt fits of each line was typically less than 2% for CO_2 lines (bottom of Fig. 4) and less than 5% for CO lines (Fig. 5), confirming the general appropriateness of the Voigt line shape model for this application.

3.2 Filtering

Subsequent to fitting the absorbance measurements, radial profiles of projected absorbance area, $A_{j,proj}(r)$, are obtained for each height x above the jet exit. Figure 6 shows example plots of $A_{j,proj}(r)$ as a function of distance from the flame center r at $x = 120$ mm. Since both the fitting residuals (bottom of Figs. 4, 5) and the absorbance uncertainties (Appendix) are much less than the observed spatial variations in $A_{j,proj}(r)$, the oscillations in measured $A_{j,proj}(r)$ are interpreted as primarily flow field variations due to the turbulence rather than measurement noise. Here, we applied a Savitzky–Golay filter [33] which smooths $A_{j,proj}(r)$ with a 1st degree polynomial inside a smoothing window size of 15 points. These smoothing parameters correspond to an effective spatial resolution of 0.55 mm, similar to the diameter

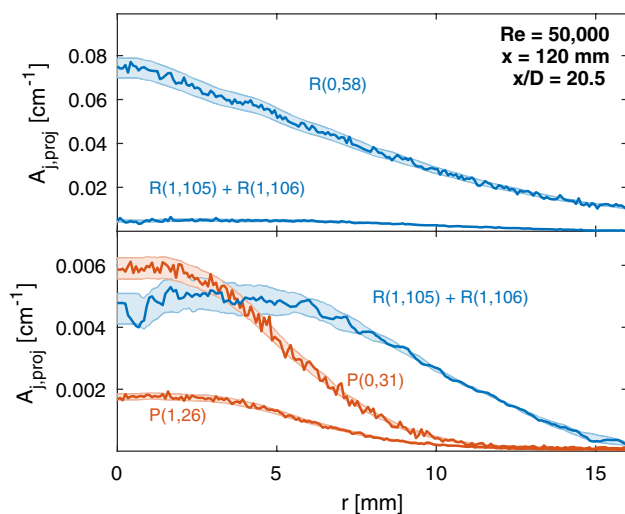


Fig. 6 Projected integrated absorbance area, $A_{j,proj}$ for the targeted lines in radial translation space

of the laser beam. The smoothed $A_{j,proj}(r)$ profiles, intended to represent mean values, are then used as inputs for tomographic reconstruction, detailed in the following section.

3.3 Tomographic reconstruction

Here, we briefly describe our approach to obtaining radial profiles of species and temperature from our path-integrated measurements. Assuming the flame is axisymmetric and steady, one-dimensional tomographic reconstruction can be applied. The projected absorbance area measurement is described by the well-known Abel transform as a line-of-sight integration over the flame with radius R at a given distance from the flame center y :

$$P(y) = 2 \int_y^R \frac{f(r)r}{\sqrt{r^2 - y^2}} dr, \tag{5}$$

where $P(y)$ is the measured projected absorbance area $A_{j,proj}(r)$ and $f(r)$ is the radial distribution of the integrated spectral absorption coefficient $K_j(r)$.

In practice, Abel inversion is implemented numerically [24]. The flame region is divided into equally spaced annular rings and the radial absorption coefficient distribution $f(r)$ is approximated by a quadratic function near radius r using the Abel 3-point (ATP) method [23]. Writing Eq. 2 at each radius r gives rise to a system of linear equations represented by

$$\mathbf{A}_{ATP} \mathbf{f} = \mathbf{P}, \tag{6}$$

where $\mathbf{f} = [f_0, f_1, \dots, f_{N-1}]^T$ and $\mathbf{P} = [P_0, P_1, \dots, P_{N-1}]^T$ contain the radial absorption coefficient values and projected absorbance area values, respectively.

In this work, the measured projected absorbance areas are deconvoluted using Tikhonov regularized Abel inversion [24] to address the inherent ill-conditioned nature of the projection matrix \mathbf{A}_{ATP} . In this method, an additional set of equations are imposed on the solution:

$$\lambda \mathbf{L}_0 \mathbf{f} = 0, \tag{7}$$

where λ is the regularization parameter that controls the level of regularization and \mathbf{L}_0 is a discrete gradient operator that characterizes the smoothness of the solution:

$$\mathbf{L}_0 = \begin{bmatrix} 1 & -1 & 0 & \dots & 0 \\ 0 & 1 & -1 & \dots & 0 \\ \dots & \dots & \dots & \dots & \dots \\ 0 & 0 & \dots & \dots & -1 \\ 0 & 0 & 0 & \dots & 1 \end{bmatrix}. \tag{8}$$

The regularization parameter λ characterizes the relative importance of the accuracy and smoothness of the solution.

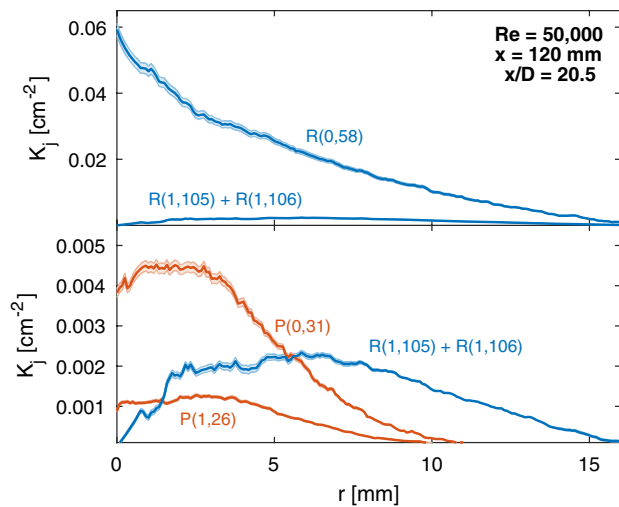


Fig. 7 Abel-inverted absorption coefficient, $K_j(r)$ for the same lines as in Fig. 6 in radial translation space

A suitable regularization parameter is determined from the L -curve method [34] to be $\lambda \approx 1$ based on the work of Daun et al. [24] and is used for all reconstructions. Combining Eqs. 6 and 7, the radial distribution $f(r)$ can be found from a least-squares solution:

$$\mathbf{f}_\lambda = \arg \min \left\| \begin{bmatrix} \mathbf{A}_{\text{ATP}} \\ \lambda \mathbf{L}_0 \end{bmatrix} \mathbf{f} - \begin{bmatrix} \mathbf{P} \\ 0 \end{bmatrix} \right\|. \quad (9)$$

Using the procedure discussed above, projected absorbance areas $A_{j,\text{proj}}(r)$ for measured spectral lines are Abel-inverted using Tikhonov regularization to reconstruct radially resolved integrated spectral absorption coefficients $K_j(r)$. Examples of these reconstructions are shown in Fig. 7. From these reconstructed absorption coefficients, temperature is calculated from the ratio of two lines at each radial position, and mole fraction is then calculated from one absorption coefficient of each species [19].

4 Results

Some example results from the jet flame experiments are plotted in the figures that follow. We first present radially resolved mole fraction measurements at two different heights (x) above the jet exit for both turbulent flow conditions. Then, we present the temperature measurements for the same planes and flow conditions. Finally, we present some composite two-dimensional images comprising the mole fraction and temperature measurements for sections of both flames. For the results shown, we use the convention of plotting distances in terms of jet diameter D ; radial distance is plotted as r/D and axial distance is plotted as x/D .

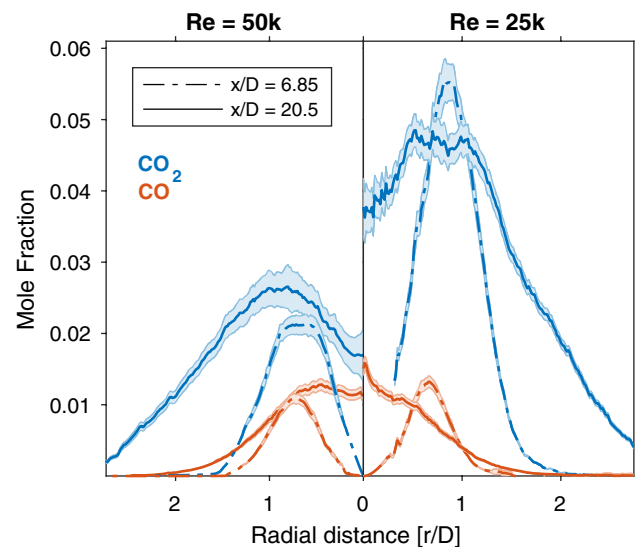


Fig. 8 Radial profiles of CO_2 and CO mole fraction calculated from Abel-inverted absorption coefficients for $Re = 50,000$ (left) and $25,000$ (right). Dashed-dotted lines indicate $x = 40$ mm ($x/D = 6.85$) and solid lines indicate $x = 120$ mm ($x/D = 20.5$). Shaded regions indicate uncertainty

4.1 Mole fraction results

The radial profiles of mole fractions for CO_2 and CO are shown for two different heights above the jet exit for the two different turbulent flow conditions in Fig. 8. For the lower plane of 40 mm ($x/D = 6.85$) in the $Re = 50,000$ case, the absorbance in the $R(1,105) + R(1,106)$ doublet line—which is typically only observed above ~ 1000 K due to the high lower state energy—was too weak to independently determine the temperature of the local CO_2 molecules. In this case, the CO temperature (and associated uncertainty in temperature) was assumed to calculate mole fraction for both species.

At the lower height of 40 mm ($x/D = 6.85$), CO and CO_2 are concentrated at a radial distance corresponding to the diameter of the jet D for both turbulent flow conditions. At the higher plane of 120 mm ($x/D = 20.5$), both the CO and the CO_2 diffuse in both the positive and negative radial directions. However, while the overall mole fractions of CO are similar at the chosen heights, the CO_2 mole fractions are much higher for the case in which the Reynolds number is 25,000 than for the case in which it is 50,000. This could either indicate greater entrainment of the outer co-flow, or more likely less complete oxidation of the fuel associated with the higher jet velocity (at higher Re) and finite rate kinetics. The temperature results that follow—along with the two-dimensional images—support the latter. For both species, typical mole fraction uncertainty is $\pm 6\%$.

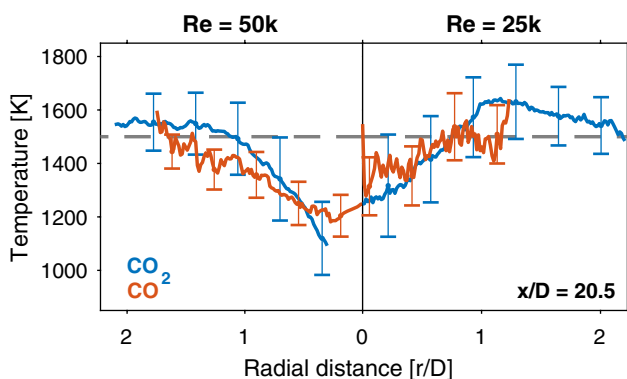


Fig. 9 Radial profiles of CO₂ and CO temperature calculated from Abel-inverted absorption coefficients for *Re* = 50,000 (left) and 25,000 (right) at *x* = 120 mm. Gray dashed lines indicate H₂/air co-flow temperature of 1500 K

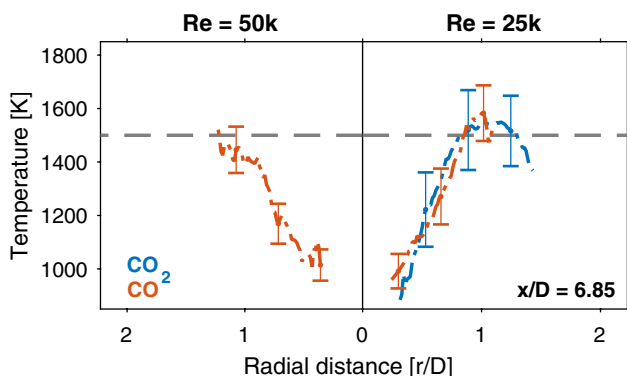


Fig. 10 Radial profiles of CO₂ and CO temperature calculated from Abel-inverted absorption coefficients for *Re* = 50,000 (left) and 25,000 (right) at *x* = 40 mm. Gray dashed lines indicate H₂/air co-flow temperature of 1500 K

4.2 Temperature results

The radial profiles of temperatures for CO₂ and CO are shown for the same distinct heights above the jet exit for the two different turbulent flow conditions in Figs. 9 and 10. As previously mentioned, for the lower plane of 40 mm (*x* / *D* = 6.85) in the *Re* = 50,000 case, the absorbance in the R(1,105) + R(1,106) doublet line was too weak to independently determine the temperature of the local CO₂ molecules and so this is not shown. Additionally, the regions in which the concentrations of CO₂ and/or CO were too low to reliably determine temperature are also not plotted. The temperature results from regions in which both CO₂ and CO are present in the flow show good agreement within experimental uncertainty. At the higher plane of *x* = 120 mm (*x* / *D* = 20.5) shown in Fig. 9, the species in the core flow have a high enough temperature and concentration for reliable

temperature measurements. The radial temperatures appear generally lower for the *Re* = 50,000 case than they are for the *Re* = 25,000 case. For the lower plane of *x* = 40 mm (*x* / *D* = 6.85) shown in Fig. 10, the difference is less clear due to the absence of high-temperature CO₂ in the *Re* = 50,000 case. However, this is consistent with a lesser degree of oxidation for this plane in the *Re* = 50,000 case. In all cases, the temperature of the molecules approaches that of the H₂/air co-flow (1500 K) as *r* / *D* increases. For the profiles shown here, typical CO temperature uncertainty is approximately ±80 K, while the uncertainty for CO₂ temperature is higher around ±130 K. The Appendix provides greater detail on uncertainty analysis.

4.3 Two-dimensional thermochemistry

In this section, we assemble the results for all planes into two-dimensional images of mole fraction and temperature for CO and CO₂ in Figs. 11, 12, 13 and 14 to reveal more about the thermochemical structure of these flames than is possible with one-dimensional radial profiles.

In Figs. 11 and 12, the mole fractions of CO₂ and CO are shown back-to-back. Both figures are plotted with the same mole fraction color scale and so are directly comparable with one another. Similarly, in Figs. 13 and 14, the

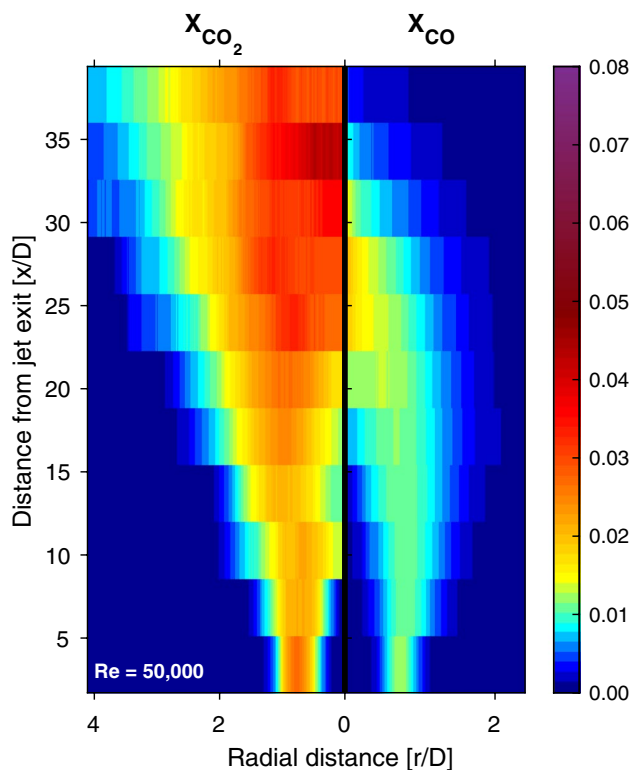


Fig. 11 Reconstructed two-dimensional mole fraction profile for species CO₂ (left) and CO (right) as a function of *r* / *D* and *x* / *D* on a C₂H₄/air jet flame. *Re* = 50,000

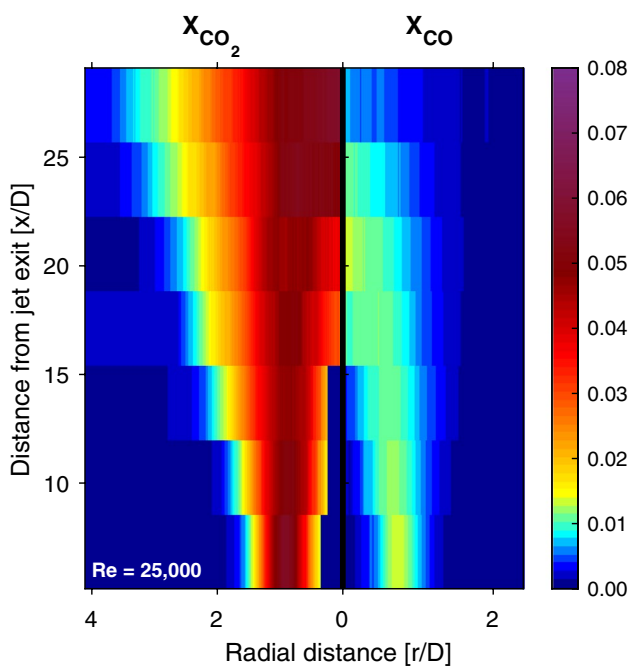


Fig. 12 Reconstructed mole fraction profile for species CO₂ (left) and CO (right) on a C₂H₄/air jet flame. *Re* = 25,000

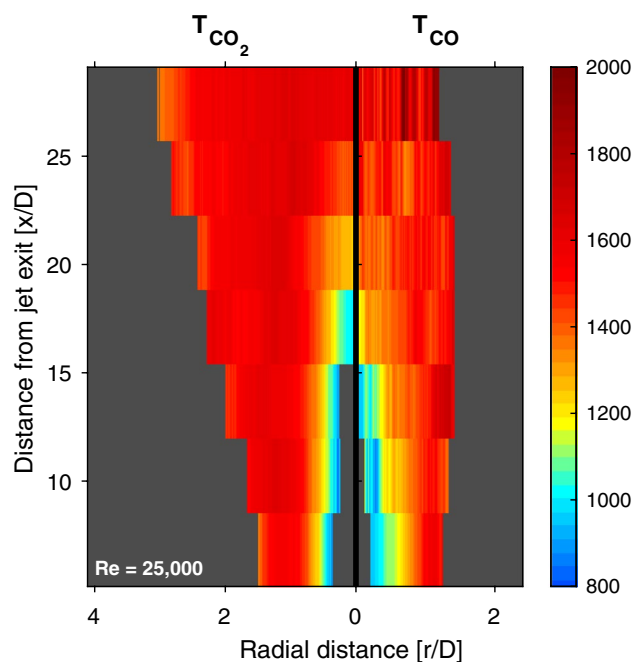


Fig. 14 Reconstructed temperature profile (Kelvin) for CO₂ (left) and CO (right) on a C₂H₄/air jet flame. *Re* = 25,000

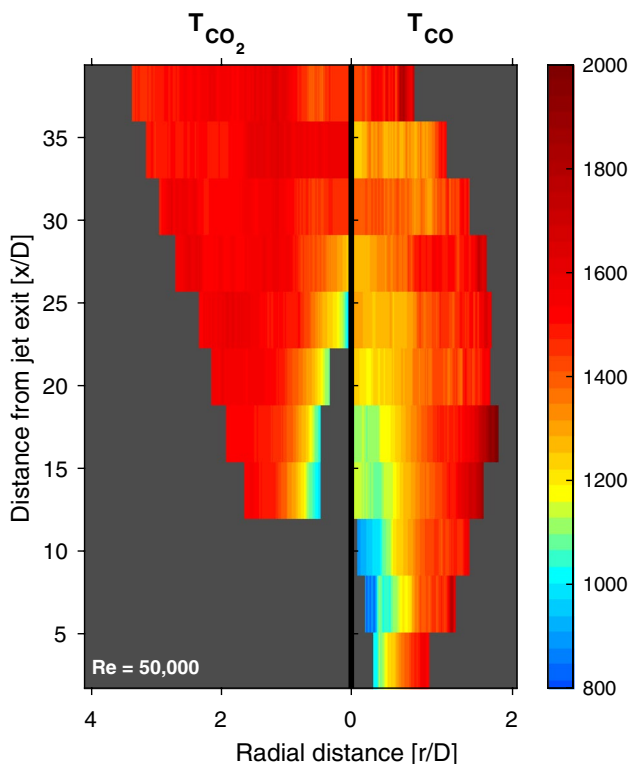


Fig. 13 Reconstructed two-dimensional temperature (in Kelvin) profile for CO₂ (left) and CO (right) as a function of *r* / *D* and *x* / *D* on a C₂H₄/air jet flame. *Re* = 50,000

temperatures of CO₂ and CO are plotted with the same temperature color scale. In all cases, the bounds of the plots are such as to maximize the view of thermochemical CO₂ and CO gradients. We again note that for the lowest three *x* / *D* planes shown in the temperature reconstruction in Fig. 12, the mole fraction of CO₂ is not measurable in the core flow due to weak absorbance in the *R*(1,105) + *R*(1,106) doublet pair in these regions. We also note again that we do not plot temperature in regions where the absorbance of one or more of the targeted spectral lines of a species is too weak (app. SNR < 5) to reliably determine temperature. Additionally, we only plot a subset of the *x* / *D* planes for the *Re* = 25,000 case, and so these plots have fewer vertical planes.

For the mole fraction images in Figs. 11 and 12, a hollow region in the core of the flame is apparent in both cases in the lower planes (particularly for CO), suggesting that fuel/air mixture in this region has yet to oxidize to either CO and CO₂. In the *Re* = 50,000 case, CO concentrations are higher in the upper planes of the flame in the core region, indicating poorer oxidation of the fuel at the tip of the flame than in the *Re* = 25,000 case. Both CO₂ and CO increase near the center of the jet as *x* / *D* increases, though only in the *Re* = 50,000 case does the CO substantially increase away from the center of the flame, as shown in Fig. 11. The overall mole fractions of CO are larger in the *Re* = 50,000 case in Fig. 11 than in the *Re* = 25,000 case in Fig. 12, while the opposite is true for the mole fractions of CO₂. In the *Re* = 50,000 case, there is higher shear present than in the *Re* = 25,000 case due to a higher velocity and momentum ratio, resulting in greater

entrainment rates with the co-flow. This could increase the size of the mixing layer causing a larger turbulent mass diffusivity as the jet velocity increases and transporting the CO away from the central axis of the flame.

In the temperature images in Figs. 13 and 14, the temperature is seen to generally be lower near the core of the flame as expected, though exact core temperatures cannot be reliably determined at the lower x/D planes. The temperatures in the $Re = 25,000$ case are generally higher for given r/D near the core of the flow than they are in the $Re = 50,000$ case. Along with the CO and CO₂ mole fraction results, this corresponds to more complete oxidation in these regions for the $Re = 25,000$ case and possibly less entrainment as well.

5 Conclusions

Our results demonstrate that mid-infrared laser absorption tomography, probing the fundamental vibrational bands of CO and CO₂, can obtain quantitative, spatially resolved thermochemical data in small-diameter (sub-cm) turbulent flames. These measurements can be made calibration free and without knowledge of balance gas composition. Species profiles are fully resolved radially and, with CO and CO₂ in combination, spatially quantify in two dimensions an important terminal reaction in hydrocarbon fuel combustion. Although temperature measurements are only reported for certain regions of the flame (i.e., partially resolved), future analysis may provide expanded measurements since additional lines besides the $R(0,58)$ and $R(1,105) + R(1,106)$ doublet were accessible with the same laser, as shown in Fig. 3.

Both the measurements of mole fraction and temperature as presented in Figs. 11, 12, 13 and 14 show sensitivity to chemical kinetic progress and turbulent flow conditions (Reynolds number). Accordingly, the sensing strategy presented in this paper may be used to help develop and/or constrain turbulent combustion fluid dynamic models with detailed chemical mechanisms. To the authors' knowledge, these are the first quantitative 2D species measurements of CO and CO₂ in the canonical piloted premixed jet burner.

Acknowledgements The authors gratefully acknowledge funding from the Air Force Office of Scientific Research (Grant number FA9550-16-1-0510) under the technical monitoring of Dr. Chiping Li and from the National Science Foundation (Grant numbers CBET-1512214 and 1752516) under the technical monitoring of Dr. Song-Chang Kong. Additionally, the authors acknowledge Daniel D. Lee for the LabVIEW data acquisition assistance as well as assistance with Fig. 1. DIP acknowledges the California Alliance Postdoctoral Fellowship, funded by NSF award nos. 1306595, 1306683, 1306747, and 1306760. DIP also acknowledges Bradley S. Cage for assistance in developing the LabVIEW motor control software for the translation stage.

Appendix: uncertainty analysis

In this paper, we report values of species concentration and temperature, but it is important to note the uncertainty in these values due to various factors. For Eqs. 1–4 as well as those in this section (unless otherwise noted), we follow the Taylor series method (TSM) of uncertainty propagation [35], in which the uncertainty of a variable r , Δr , is given by:

$$(\Delta r)^2 = \left(\frac{\partial r}{\partial x_1} \Delta x_1 \right)^2 + \left(\frac{\partial r}{\partial x_2} \Delta x_2 \right)^2 + \dots, \quad (10)$$

where x_i are dependent variables and Δx_i are their respective uncertainties. As indicated by Eq. 4, mole fraction of an absorbing species $X_{\text{abs}}(r)$ depends on line strength $S_j(T(r))$ and reconstructed absorption coefficient $K_j(r)$. In turn, $S_j(T(r))$ depends on temperature $T(r)$, which itself depends on $R(r)$, which is also dependent on $K_j(r)$. We present a discussion which propagates uncertainty from initial intensity measurements I_t and I_0 through these equations to obtain uncertainty in $T(r)$ and $X_{\text{abs}}(r)$.

The systematic error in I_t and I_0 is assumed to be the same because the same system is used to measure both signals; thus, the only uncertainty considered for each of these signals is the random uncertainty among all the scans averaged within a spatial segment dr (in this case, the distance associated with 105 direct-absorption scans). For each spatial segment, the standard deviations of both the incident background I_0 and the absorbance signals I_t are calculated, which are both used to determine the 95% confidence interval of the signals, represented by ΔI_0 and ΔI_t . To obtain the variation *specifically in absorbance*, $\Delta \alpha_v$, we subtract ΔI_0 from ΔI_t and use the resulting value as a bound on absorbance signal, $I_t \pm (\Delta I_t - \Delta I_0)$. We then calculate the resulting variation in α_v , $\Delta \alpha_v$, by propagating the uncertainty in Eq. 1. This is shown in Figs. 4 and 5 as gray-shaded regions. In turn, $\Delta A_{j,\text{proj}}$ is calculated by propagating the uncertainty $\Delta \alpha_v$ in Eq. 2, generating an upper and lower bound on $A_{j,\text{proj}}$. This process occurs for each spatial interval dr across the radius of the burner r . The resulting upper and lower bounds of $A_{j,\text{proj}}(r)$ are smoothed with a Savitzky–Golay filter [33] and plotted alongside the averaged $A_{j,\text{proj}}(r)$ as shown in Fig. 6.

The uncertainty in $K_j(r)$, $\Delta K_j(r)$, is determined numerically via tomographic reconstruction of the upper and lower bounds of $A_{j,\text{proj}}(r)$. Applying Eq. 10 to Eq. 3, we can calculate the uncertainty in $R(r)$, $\Delta R(r)$:

$$\left(\frac{\Delta R(r)}{R(r)} \right)^2 = \left(\frac{\Delta K_A(r)}{K_A(r)} \right)^2 + \left(\frac{\Delta K_B(r)}{K_B(r)} \right)^2. \quad (11)$$

The ratio $R(r)$ is used to determine temperature $T(r)$ via the following equation:

$$T(r) = \frac{\frac{hc}{k_B}(E''_A - E''_B)}{\ln(R(r)) + \ln\left(\frac{S_B(T_0)}{S_A(T_0)}\right) + \frac{hc}{k_B}\frac{(E''_A - E''_B)}{T_0}}. \quad (12)$$

Here, h [J·s] is the Planck constant, c [cm/s] is the speed of light, k_B [J/K] is the Boltzmann constant, and E''_j [cm⁻¹] is the lower state energy for the two lines A and B. Since $T(r)$ is a function of $R(r)$, there is an associated uncertainty in temperature, $\Delta T(r)$. Using Eq. 10 in Eq. 12, $\Delta T(r)$ is given by:

$$\frac{\Delta T(r)^2}{T(r)^2} = \frac{(\Delta R(r)/R(r))^2 + (\Delta S_B(T_0)/S_B(T_0))^2 + (\Delta S_A(T_0)/S_A(T_0))^2}{\left(\ln(R(r)) + \ln\left(\frac{S_B(T_0)}{S_A(T_0)}\right) + \frac{hc}{k_B}\frac{(E''_A - E''_B)}{T_0}\right)^2}. \quad (13)$$

As mentioned, $S_j(T(r))$ is function of $T(r)$ [19]:

$$S_j(T) = S_j(T_0) \frac{Q(T_0)}{Q(T)} \frac{T_0}{T} \exp\left[-\frac{hcE''_j}{k_B}\left(\frac{1}{T} - \frac{1}{T_0}\right)\right] \times \left[1 - \exp\left(-\frac{hcv_{0,j}}{k_B T}\right)\right] \left[1 - \exp\left(-\frac{hcv_{0,j}}{k_B T_0}\right)\right]^{-1}, \quad (14)$$

where it is understood that T is $T(r)$. Q is the partition function for the internal energy modes of the molecule. Therefore, $\Delta T(r)$ (from the uncertainty in $\Delta R(r)$) affects $S_j(T(r))$ which is used to calculate mole fraction. The following expression can be obtained for the uncertainty in line strength due to uncertainty in observed temperature, $\Delta T(r)$:

$$\Delta S_{j,T}^2(T) = S_j^2(T) \Delta T^2 \left(-\frac{\partial Q(T)/\partial T}{Q(T)} - \frac{1}{T} + \frac{hcE''_j}{k_B T^2} + \frac{hcv_{0,j}}{k_B T^2} \left(\frac{\exp(-hcv_{0,j}/k_B T)}{1 - \exp(-hcv_{0,j}/k_B T)} \right) \right)^2. \quad (15)$$

This expression is consistent with the analysis presented by Ouyang and Varghese [36]. For our experimental results, the line strength uncertainty is proportional to the line strength itself. Additionally, the HITRAN database reports inherent uncertainty in $S_j(T_0)$ (2% for all spectral lines in this work), which we refer to here as $\Delta S_j(T_0)$. Thus, the total uncertainty in line strength can be calculated:

$$\Delta S_j^2(T) = \Delta S_{j,T}^2(T) + \Delta S_j^2(T_0). \quad (16)$$

Now, mole fraction is given by:

$$X_{\text{abs}}(r) = \frac{K_j(r)}{S_j(T(r))P}. \quad (17)$$

For our CO₂ measurements, ambient CO₂ in the atmosphere (approximately 400 ppm at the time of the experiment)

influences the background measurement of I_0 slightly, since there is ambient CO₂ in the H₂/air co-flow flame. Thus, the maximum expected uncertainty due to ambient concentrations of the species, $\Delta X_{\text{abs, amb}}$, is 400 ppm for CO₂, or $\Delta X_{\text{CO}_2} = 0.0004$, which is less significant than the other sources of uncertainty. Utilizing Eq. 10, the uncertainty in mole fraction, excluding uncertainty in total pressure P , is:

$$\left(\frac{\Delta X_{\text{abs}}(r)}{X_{\text{abs}}(r)}\right)^2 = \left(\frac{\Delta K_j(r)}{K_j(r)}\right)^2 + \left(\frac{\Delta S_j(T(r))}{S_j(T(r))}\right)^2 + \left(\frac{\Delta X_{\text{abs, amb}}(r)}{X_{\text{abs}}(r)}\right)^2. \quad (18)$$

Thus, the uncertainties in $\Delta K_j(r)$ and $\Delta S_j(T(r))$ accounted for. Eqs. 13 and 18 are used to calculate the error bounds in Figs. 8, 9, and 10.

References

1. E.D. Gonzalez-Juez, A.R. Kerstein, R. Ranjan, S. Menon, *Prog. Energy Combust. Sci.* **60**, 26–67 (2017)
2. S.B. Pope, *Proc. Combust. Inst.* **34**, 1–31 (2013)
3. A.R. Masri, R.W. Dibble, R.S. Barlow, *Prog. Energy Combust. Sci.* **22**, 307–362 (1996)
4. M.J. Dunn, A.R. Masri, R.W. Bilger, *Combust. Flame* **151**, 46–60 (2007)
5. M.J. Dunn, A.R. Masri, R.W. Bilger, R.S. Barlow, G.H. Wang, *Proc. Combust. Inst.* **32**(II), 1779–1786 (2009)
6. F. Fuest, R.S. Barlow, G. Magnotti, J.A. Sutton, *Combust. Flame* **188**, 41–65 (2018)
7. T.A. McManus, J.A. Sutton, *Quantitative 2D temperature imaging in turbulent nonpremixed jet flames using filtered Rayleigh Scattering*, in *55th AIAA Aerosp. Sci. Meet.* (American Institute of Aeronautics and Astronautics, Reston, 2017)
8. I. Trueba Monje, J.A. Sutton, *Filtered Rayleigh scattering thermometry in premixed flames*, in *2018 AIAA Aerosp. Sci. Meet.* (American Institute of Aeronautics and Astronautics, Reston, 2018)
9. V. Bergmann, W. Meier, D. Wolff, W. Stricker, *Appl. Phys. B* **66**, 489–502 (1998)
10. W. Meier, R.S. Barlow, Y.L. Chen, J.-Y. Chen, *Combust. Flame* **123**, 326–343 (2000)
11. R. Cabra, J. Chen, R. Dibble, A. Karpets, R. Barlow, *Combust. Flame* **143**, 491–506 (2005)
12. D. Veynante, L. Vervisch, *Prog. Energy Combust. Sci.* **28**, 193–266 (2002)
13. D. Han, A. Satija, J. Kim, Y. Weng, J.P. Gore, R.P. Lucht, *Combust. Flame* **181**, 239–250 (2017)
14. R.S. Barlow, G.H. Wang, P. Anselmo-Filho, M.S. Sweeney, S. Hochgreb, *Proc. Combust. Inst.*, **32**(I), 945–953 (2009)
15. M.J. Dunn, A.R. Masri, R.W. Bilger, R.S. Barlow, *Flow Turbul. Combust.* **85**, 621–648 (2010)
16. B.R. Halls, J.R. Gord, T.R. Meyer, D.J. Thul, M. Slipchenko, S. Roy, *Proc. Combust. Inst.* **36**, 4611–4618 (2017)
17. J. Smolke, S. Lapointe, L. Paxton, G. Blanquart, F. Carbone, A.M. Fincham, F.N. Egolfopoulos, *Proc. Combust. Inst.* **36**, 1877–1884 (2017)
18. F. Carbone, J.L. Smolke, A.M. Fincham, F.N. Egolfopoulos, *Combust. Flame* **180**, 88–101 (2017)
19. R.K. Hanson, R.M. Spearrin, C.S. Goldenstein, *Spectroscopy and Optical Diagnostics for Gases* (Springer, New York, 2016)

20. C.S. Goldenstein, R.M. Spearrin, J.B. Jeffries, R.K. Hanson, *Prog. Energy Combust. Sci.* **60**, 132–176 (2017)
21. L.S. Rothman, I.E. Gordon, R.J. Barber, H. Dothe, R.R. Gamache, A. Goldman, V.I. Perevalov, S.A. Tashkun, J. Tennyson, *J. Quant. Spectrosc. Radiat. Transf.* **111**, 2139–2150 (2010)
22. J.J. Girard, R.M. Spearrin, C.S. Goldenstein, R.K. Hanson, *Combust. Flame* **178**, 158–167 (2017)
23. C.J. Dasch, *Appl. Opt.* **31**, 1146–1152 (1992)
24. K.J. Daun, K.A. Thomson, F. Liu, G.J. Smallwood, *Appl. Opt.* **45**, 4638–4646 (2006)
25. M. Ravichandran, F.C. Gouldin, *Combust. Sci. Technol.* **60**, 231–248 (1988)
26. R. Villarreal, P.L. Varghese, *Appl. Opt.* **44**, 6786–6795 (2005)
27. L. Ma, W. Cai, A.W. Caswell, T. Kraetschmer, S.T. Sanders, S. Roy, J.R. Gord, *Opt. Express* **17**, 8602–8613 (2009)
28. J. Song, Y. Hong, G. Wang, H. Pan, *Appl. Phys. B* **112**, 529–537 (2013)
29. P. Nau, J. Koppmann, A. Lackner, K. Kohse-Höinghaus, A. Brockhinke, *Appl. Phys. B* **118**, 361–368 (2015)
30. J. Foo, P.A. Martin, *Appl. Phys. B* **123**, 160 (2017)
31. X. Liu, G. Zhang, Y. Huang, Y. Wang, F. Qi, *Appl. Phys. B* **124**, 61 (2018)
32. D.D. Lee, F.A. Bendana, S.A. Schumaker, R.M. Spearrin, *Appl. Phys. B* **124**, 77 (2018)
33. A. Savitzky, M.J.E. Golay, *Anal. Chem.* **36**, 1627–1639 (1964)
34. P.C. Hansen, *Rank-deficient and discrete Ill-posed problems: Numerical aspects of linear inversion* (Society for Industrial Mathematics, 1987)
35. H.W. Coleman, W.G. Steele, *Experimentation, validation, and uncertainty analysis for engineers*, 3rd edn. (Wiley, Hoboken, 2009)
36. X. Ouyang, P.L. Varghese, *Appl. Opt.* **28**, 3979–3984 (1989)